2 Scanning Probe Microscopy: From Living Cells to the Subatomic Range

Ille C. Gebeshuber · Manfred Drack · Friedrich Aumayr · Hannspeter Winter · Friedrich Franek

Abbreviations

AFM	atomic force microscopy
ATP	adenosine triphosphate
BDPA	a, g-bisdiphenylene b-phenylallyl
CDOS	charge density-of-states
ESD	electron stimulated desorption
HOPG	highly oriented pyrolytic graphite
ID	interstitial defect
MCI	multiply charged ion
MEMS	microelectromechanical system
MR	magnetic resonance
MRFM	magnetic resonance force microscopy
MRI	magnetic resonance imaging
NEMS	nanoelectromechanical systems
PS	potential sputtering
PSD	photon stimulated desorption
rms	root mean square
SEM	scanning electron microscopy
SPM	scanning probe microscopy
UHV	ultra-high vacuum
VD	vacancy defect

2.1 Introduction

In this chapter the reader will be introduced to scanning probe microscopy of samples varying by seven orders of magnitude in size (Fig. 2.1). The largest samples presented are living cells, measuring some hundreds of micrometers. Small units of life, biomolecules with only some tens of nanometers, are the next sample. They are investigated while interacting with each other in real-time. One more step down in size, small ion induced defects on atomically flat crystals represent structures in the nanometer regime. New data storage devices might result from such investigations. Finally, single electron spin detection (dozens of atomic layers beneath the surface) and the imaging of atom orbitals extend scanning probe microscopy to the subatomic regime. 3D atomic-level information of (bio)molecules embedded in their natural

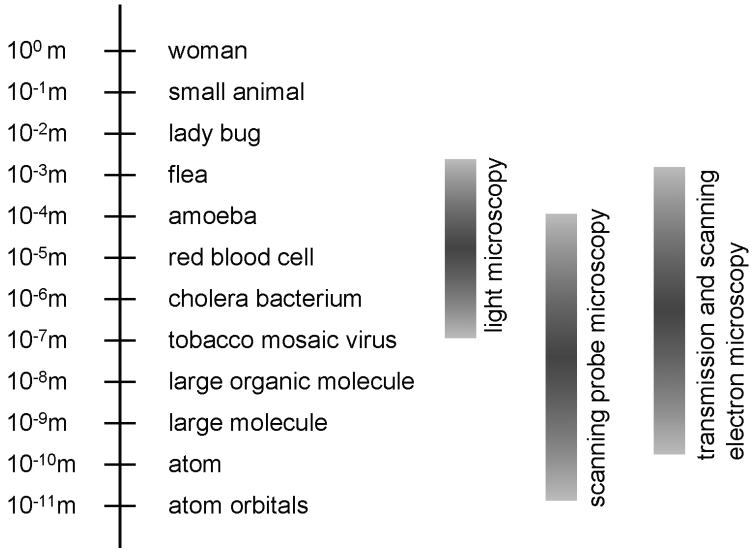

Fig. 2.1. The major types of microscopy cover at least eight orders of magnitude in size. Common examples for every scale are given. Note that scanning probe microscopy covers seven orders of magnitude

environment or single defect imaging in bulk silicon might be possible with these new techniques in the near future.

These versatile applications demand methods such as scanning tunneling microscopy at ultra-low temperatures (1.6 K) or atomic force microscopy in ultra-high vacuum (10^{-11} mbar). Furthermore, in many cases, specially engineered and/or functionalized scanning probe tips are needed.

2.2 Cells In Vivo as Exemplified by Diatoms

Manfred Radmacher [1] gives an excellent overview on the investigation of living cells by atomic force microscopy in the preceding chapter. To this, we add a remarkable group of organisms: diatoms.

2.2.1 Introduction to Diatoms

Diatoms [2] are unicellular microalgae with a cell wall consisting of a siliceous skeleton enveloped by an organic case essentially composed of polysaccharides and proteins [3].

Diatoms are small, mostly easy to cultivate, highly reproductive and, since many of them are transparent, they are accessible by different kinds of optical microscopy methods.

The cell walls form a pillbox-like shell (siliceous exoskeleton). This shell consists of two valves and a series of girdle bands. Diatoms vary greatly in shape, ranging from box-shaped to cylindrical; they can be symmetrical as well as asymmetrical and exhibit an amazing diversity of nanostructured frameworks (Fig. 2.2).

These naturally nanostructured surfaces gained the attention of nanoscientists, and diatom nanotechnology developed as a new interdisciplinary field of research [4].

Diatoms are found in freshwater, brackish and marine environments, as well as in moist soils, and on other regularly moist surfaces. They are either freely floating (planktonic forms) or attached to a substratum (benthic forms), and some species may form colonies in the form of chains of cells of varying length. Individual diatoms range from two micrometers up to several millimeters in size, although only few species are larger than 200 micrometers. Diatoms as a group are very diverse with 12,000 to 60,000 species reported [6, 7].

These unicellular organisms are interesting from the point of view of materials science and biomimetic studies, since they master challenges as diverse as building nanostructured glass shells with high load capacity (a problem interesting for light-weight structures architecture) and engineering strong and robust adhesives that are stable in wet environments (most man-made adhesives fail to bond in wet conditions, owing to chemical modification of the adhesive or its substrate). Furthermore, diatoms excel at preventing dissolution of their silica shells in water owing to a covering layer (up-to-date technology is currently facing the problem that man made glass fiber reinforced polymers show rapid deterioration when used in water).

Currently, human chemical synthesis cannot produce siliceous structures with the hierarchical structural detail of the diatom frustules nor can ordered siliceous

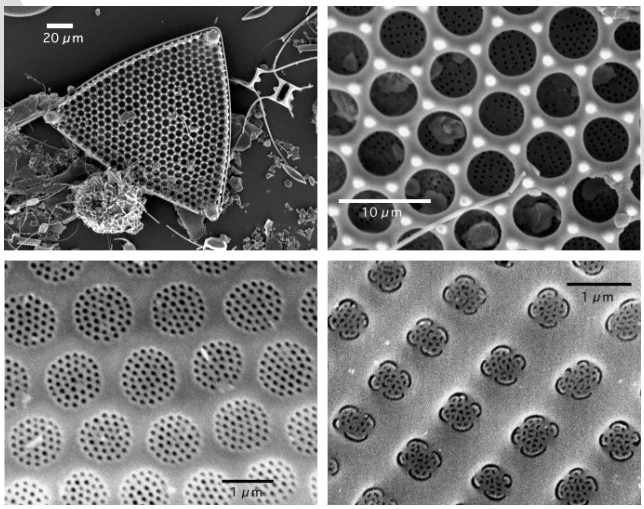

Fig. 2.2. Siliceous exoskeletons of three diatom species imaged with scanning electron microscopy. *Top*: *Tricaeratium favus*, whole cell (*left*), detail (*right*). *Bottom*: *Roperia tessellata* (*left*) and *Achnathes brevipes* (*right*). Reprinted with permission from Gebeshuber IC, Thompson JB, Del Amo Y, Stachelberger H, Kindt JH (2002) Mat Sci Technol 18:763 [5] © 2002 IoM Communications Ltd.

structures be produced synthetically under the benign conditions of diatom biomineralization. Biosilicification occurs at ambient temperatures and pressures, whereas artificial chemical synthesis of silica-based materials (e.g. resins, molecular sieves and catalysts) requires extreme conditions of temperature, pressure and pH.

2.2.2 SPM of Diatoms

The first AFM study of diatoms was presented in 1992 [8]. In this study, the surface structure of six different diatom species collected from a mud sample was imaged after the cells had been briefly rinsed with ethanol to kill, clean and immobilize them.

Topography and micromechanical properties like elasticity and hardness of dead diatom cells were reported by Almquist et al. in 2001 [9].

In contrast to these AFM images of dead cells, topography and micromechanical properties (such as viscoeleastic properties, adhesion forces and hardness) of the surface of the living diatom cell has been investigated [e.g. 5, 10–13].

Lee and co-workers combined scanning electrochemical microscopy and scanning optical microscopy to obtain simultaneous electrochemical and optical images of living diatoms in a constant-current mode [14]. This kind of microscopy might prove useful in mapping the biochemical activity of a living cell.

The defense potential of the diatom shell was investigated by Hamm and co-workers by measuring its strength [15]. It was found that diatoms are remarkably strong by virtue of their architecture and the material properties of the diatom silica.

In 2004 Arce and co-workers used the AFM to compare the adhesion of diatoms to several surfaces. Tipless AFM cantilevers were functionalized with live diatom cells, and the surfaces investigated were tested with the same diatom bioprobe [16].

2.2.2.1 Diatom Topography as Investigated with AFM

Owing to the poor adhesion to the substrate, it is impossible to obtain stable images of most benthic diatom species with the AFM.

AFM-compatible diatom species can be selected from a large sample by following a simple and effective strategy: Freshwater aquarium plants covered with benthic diatoms are placed in a jar filled with water, as well as two left-handed European freshwater snail species, *Physa fontinalis* and *Planorbarius corneus*, and some glass slides. In the following weeks, the diatoms will colonize the jar and the glass slides. The snails will feed on the diatoms, predominantly leaving the species behind , which obviously strongly attach to the substrate.

By this strategy, Gebeshuber and co-workers selected three different diatom species: *Eunotia sudetica, Navicula seminulum* and a yet unidentified species, and subsequently imaged them in contact mode AFM (Fig. 2.3).

The natural adhesives of these diatoms, which attach them to the substrate as well as to each other (all of them are colonial forms), prove to be sufficiently strong that stable AFM imaging conditions are achieved without further sample preparation.

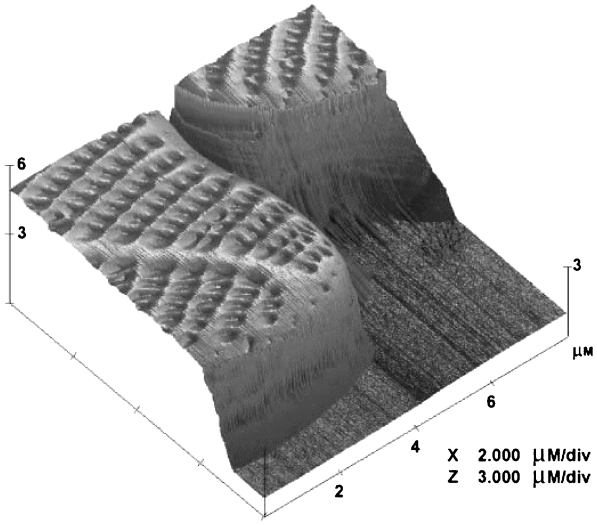

Fig. 2.3. AFM image of parts of two living diatom cells of the species *Navicula seminulum* growing on a glass slide. Note that the flat area does not correspond to the surface of the glass slide, but is determined by the maximum possible extension of the z-piezo of the microscope. Image acquired using AFM contact-mode imaging in water, imaging parameter topography, scan size $8 \times 8\ \mu m^2$, scanning frequency 1 Hz. Reprinted with permission from Gebeshuber IC, Kindt JH, Thompson JB, Del Amo Y, Stachelberger H, Brzezinski M, Stucky, GD, Morse DE, Hansma PK (2003) J Microsc 212:292 [12] © 2003, The Royal Microscopical Society

The cells are imaged in their culture medium or in tap water while they are still growing on the glass slides. Tapping-mode as well as contact mode imaging is easy to achieve as long as engaging the cantilever takes place on the cell surface.

Navicula seminulum grows in stacks of cells pointing out from the glass slide. These chains of cells can be about 10 cells high, as investigated by SEM (data not shown). Figure 2.3 reveals detailed surface patterning of the top valve faces of two adjacent cells of *Navicula seminulum*.

The chains of *Eunotia sudetica* and of the yet unidentified species grow with the valve faces perpendicular to the surface of the glass slide, allowing for AFM investigation of the girdle bands.

The cells are alive and continue to divide after imaging.

2.2.2.2 Diatom Adhesives Investigated by SPM

Most man-made adhesives fail to bond in wet conditions, owing to chemical modification of the adhesive or its substrate. Engineering strong and robust underwater adhesives that are stable in wet environments is a challenge to current technology. Diatoms produce excellent adhesives that are stable and robust in wet environments.

Phase images depict the phase delay between the drive and response of the cantilever. These images contain information about the energy dissipated during

the interaction of the AFM tip with the sample, and can help us to understand the viscoelastic and adhesion properties of the surfaces investigated, specifically of the organic material responsible for diatom adhesion.

Because phase imaging highlights edges and is not affected by large-scale height differences, it provides clearer observation of fine features that can be hidden by rough topography (Fig. 2.4). To investigate the natural adhesives utilized to attach cells to each other and to the substratum, it was tried to probe the cleft between two connected diatom cells with the AFM. In the yet unidentified species, the cleft at the cell–cell interface proved too deep. In this region, even the use of electron-beam-deposited AFM tips with high aspect ratio merely results in tip imaging. Phase imaging reveals slight differences (2°) in viscoelastic and adhesion properties of the two adjacent valves. *Eunotia sudetica*, by contrast, is very convenient for *in situ* investigation of the diatom adhesive at the cell interface, because there is barely any cleft between adjacent cells and valve undulations are less pronounced

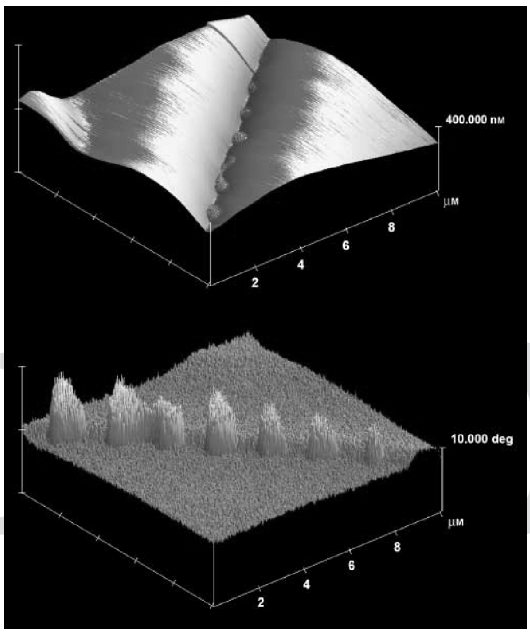

Fig. 2.4. (**a**) The adhesives in the contact region of two cells of *Eunotia sudetica* are apparent as small topographic features on the slightly undulated cell interface. The corrugation of the bead-like structures is between 10 and 20 nm, and their lateral dimension and spacing is about 1 mm. (**b**) In the phase image these features are far more striking. The diatom adhesive causes a phase lag of about 10° compared with the rest of the frustule surfaces, where on a single frustule it is within 1°. Note the 2° interfrustule phase step, which reveals slightly different viscoelastic properties of the two neighboring valves. Tapping mode, topography and phase, scan size $10 \times 10\ \mathrm{mm}^2$, scan rate 5 Hz. Note that for better view (**b**) is rotated clockwise by 90° as compared with (**a**). Reprinted with permission from Gebeshuber IC, Kindt JH, Thompson JB, Del Amo Y, Stachelberger H, Brzezinski M, Stucky, GD, Morse DE, Hansma PK (2003) J Microsc 212:292 [12] © 2003, The Royal Microscopical Society

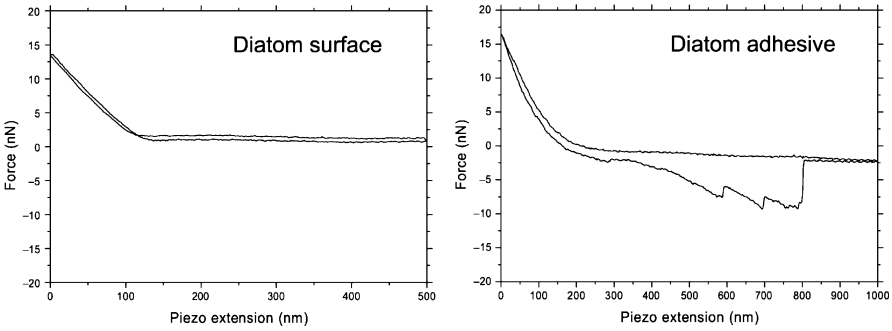

Fig. 2.5. Force–distance curves. *Left*: no adhesion can be recognized on the diatom surface. *Right*: representative data for the diatom adhesive that attaches *Eunotia sudetica* to the substrate. Several debonding events occur. Reprinted with permission from Gebeshuber IC, Kindt JH, Thompson JB, Del Amo Y, Stachelberger H, Brzezinski M, Stucky, GD, Morse DE, Hansma PK (2003) J Microsc 212:292 [12] © 2003, The Royal Microscopical Society

than in the other species investigated (Fig. 2.4). The diatom adhesive is apparent as small topographic features at the cell interface. The bead-like structures are 10–20 nm high, have lateral dimensions of about 1 μm and are about 1 μm apart. The phase image clearly depicts the altered viscoelastic properties of these structures: the diatom adhesive causes a phase difference of up to 10° compared with the phase difference on the rest of each of the two frustules, where it is within 1° on each, apart from a 2° phase difference between the two adjacent valves, a feature which also appears in the other species, where the adhesives are not accessible because of deep clefts between the single organisms.

Force–distance curves on the surface and on the adhesive of *Eunotia sudetica* reveal basic differences in adhesion properties (Fig. 2.5). On the diatom surface, no adhesion force can be detected (Fig. 2.5 left). The diatom adhesive, by contrast, is strong and robust in the wet environment. To gain reproducible access to this natural adhesive, a chain of *Eunotia sudetica* that was embedded in a densely packed field of *Navicula seminulum* was scraped away from the glass slide with an STM-tip mounted on a three-dimensional micromanipulator. Over a period of several hours, force–distance curves were taken on the adhesive molecules that were used to attach the diatom cells to the glass slide (Fig. 2.5, right). No change in the basic shape of the force–distance curves can be detected within hours of repetitive pulling in the area where the colony was located. Typically, several debonding events occur until the natural adhesive molecules finally debond at a tip–surface separation of about 600 nm. For a detailed description of this study, see [5, 11].

2.3 Interaction of Large Organic Molecules

Conformational diseases such as Parkinson's disease, Alzheimer's disease, kuru, scrapie, BSE and vCJD (variant Creutzfeldt-Jakob Disease) result from misfolded proteins aggregating into detrimental structures like amyloid fibers [18–20].

The amount of protein involved ranges from scarcely detectable to kilograms.

Partial unfolding might expose significant regions of the polypeptide chain to the outside world, allowing the protein to aggregate and convert into amyloid fibrils. Once formed, the strong hydrogen bonding between molecules can make this process effectively irreversible.

As with crystallization, the formation of amyloid fibrils is "seeded" by preformed aggregates, a phenomenon that might also be responsible for the rapid progression of sporadic diseases such as Alzheimer's once the symptoms become evident. BSE, for example, has almost undoubtedly resulted from the highly unnatural practice of feeding young cows on the remains of old ones, with the disease then being transmitted to humans as vCJD. Both kuru and BSE have virtually disappeared as a result of effective action taken once their origins were understood.

The proteins that have emerged under evolutionary pressure are normally robust enough to resist reversion to aggregated states. Evolutionary processes have selected sequences of amino acids with the remarkable ability to form monomeric structures in which the main chain is folded in a unique way within the mass of close-packed side chains, preventing it from interacting with other molecules.

Furthermore, "chaperone" proteins help to protect against such changes.

Chaperones are proteins whose function is to assist other proteins in achieving proper folding: They prevent protein aggregation by providing encapsulated hydrophobic environments that allow the protein to fold properly.

Many chaperones are heat or cold shock proteins, that is, proteins expressed in heat or cold shock conditions. The reason for this behavior is that protein folding is severely affected by extreme temperatures. Chaperones act to counteract the potential damage. Although most proteins can fold in the absence of chaperones, a minority strictly requires them.

A large number of chaperones need adenosine triphosphate (ATP) to function properly. Chaperones recognize unfolded proteins by the hydrophobic residues these expose to the solvent. Exposed hydrophobic residues are unusual for properly folded proteins. Since the environment of the cell is characterized by hydrophilic groups (mostly water), incompletely folded or misfolded proteins with exposed hydrophobic groups have a tendency to aggregate to larger structures, where again, the hydrophobic residues would be hidden from the surrounding.

Chaperonins are a subset of chaperone proteins found in prokaryotes, mitochondria and plastids.

The AFM has proven to be a useful tool for studying proteins at the single molecule level. For a review on single molecule techniques in biomedicine and pharmacology, see [21].

Many of the single molecule studies with the AFM have been restricted by noise and speed limitations.

The first protein–protein interactions on the single molecule level imaged in real time were presented in 2000 [22]. This study demonstrated the enormous contributions AFM can make to molecular biology. Bulk results are interesting, but there are many valuable properties that can only be investigated on the single molecule level.

This work was enabled by the development of small cantilevers [23–25]. Small cantilevers allow for faster imaging and faster force spectroscopy of single biopo-

lymers, because they have higher resonant frequencies and lower coefficients of viscous damping.

A new generation of AFMs using small cantilevers will enable the study of biological processes with greater time resolution, possibly at video refresh rates. Furthermore, small cantilever AFMs allow to narrow the gap in time between results from force spectroscopy experiments and molecular dynamics calculations.

The small cantilevers are fabricated out of low stress silicon nitride. They are ten micrometers long, have widths of 3–5 mm, and their thickness is about 75 nm. These cantilevers can measure smaller forces than larger cantilevers with the same spring constant because they have lower coefficients of viscous damping.

The prototype small AFM detects the motion of small cantilevers by using high numerical aperture optics to focus a laser beam onto the cantilever and then measuring angular changes in the reflected light beam.

This microscopy was used to observe, in real time, the interactions between individual molecules of the *Escherichia coli* chaperonin protein GroES binding to and then dissociating from individual *E. coli* GroEL proteins, which were immobilized on a mica support.

Both X-ray crystallography and cryoelectron microscopy studies have been used to resolve the structures of GroEL and the GroEL–GroES complex in different stages of the folding cycle (Fig. 2.6, e.g. [26–31]).

A prototype small cantilever AFM [25] image of both GroEL deposited on mica and the GroEL–GroES complex repeatedly without the aid of fixing agents (Fig. 2.7).

GroEL adsorbs to mica in end-up orientation. The average diameter of the molecules in this image agrees with the X-ray and cryoelectron microscopy data.

Upon the addition of GroES and ATP into the buffer solution, GroES molecules were observed as features that extend 3.6±1 nm higher than the GroEL film (Fig. 2.8).

The height of these features is also consistent with X-ray crystallography and cryoelectron microscopy data. The same sample region can be scanned repeatedly without excessively disturbing the GroEL–GroES complexes (for details, see [22]).

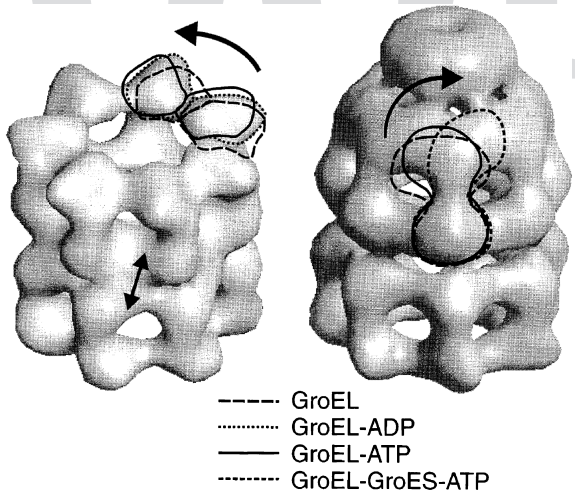

Fig. 2.6. Cryoelectron microscopy images of GroEL (*left*) and the GroEL–GroES complex. The height of the GroEL molecule is about 15.1 nm, the height of the GroEL–ES complex is about 18.4 nm. Upon interaction with ADP or ATP, domain movements occur, as indicated. Reprinted with permission from Roseman AM, Chen S, White H, Braig K, Saibil HR (1996) Cell 87:241 [31] © 1996, Elsevier

TS[1] Please check the quality of this figure.

Editor's or typesetter's annotations (will be removed before the final TEX run)

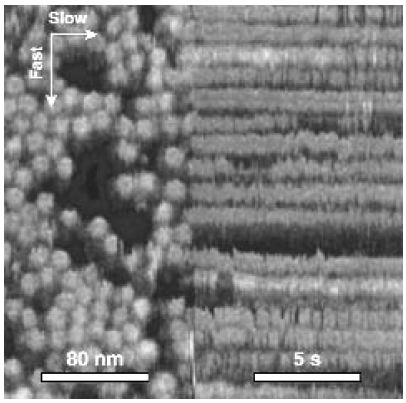

Fig. 2.7. GroEL film deposited on mica scanned in two dimensions (*left*) and in one dimension (*right*). In this image of GroEL, the movement along the slow scan axis was disabled half way through the scan. From then on the AFM tip repeatedly scanned the same line of proteins. Each *horizontal line*, therefore, shows changes in time of an individual molecule. Reprinted with permission from Viani MB, Pietrasanta LI, Thompson JB, Chand A, Gebeshuber IC, Kindt JH, Richter M, Hansma HG and Hansma PK (2000) Nature Struct Biol 7:644 [22] © 2000, Nature Publishing Group[rs1]

Therefore, in order to obtain the temporal resolution required for observing the formation and dissociation of the GroEL–GroES complexes in the presence of Mg-ATP, the sample was scanned in one dimension rather than two (Fig. 2.8).

The time/height diagram of the protein lines displays repetitive well-defined step-like variations in height (Fig. 2.8). The magnitude of these steps is 3.6 ± 1 nm. The observed height variations result from GroES molecules attaching to and then separating from the respective GroEL molecules.

Without GroES and Mg-ATP no such steps can be observed.

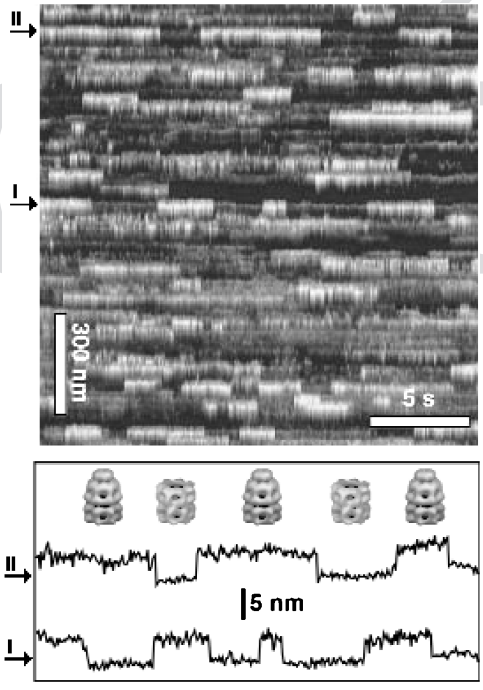

Fig. 2.8. Tapping mode AFM in liquid. *Top*: after the addition of GroES and Mg-ATP into the buffer solution, variations in height along the lengths occur in the single protein lines, as exemplified by *arrows I* and *II*. *Bottom*: time/height diagram of the protein lines indicated with the *arrows* in the top image. The height changes between two values that differ by 3.6 ± 1 nm. This indicates the binding and unbinding of GroES. The cryoelectron microscopy images of GroEL and the GroEL–GroES complex are from Roseman et al., 1996 (reprinted with permission, © 1996, Elsevier). Adapted with permission from Viani MB, Pietrasanta LI, Thompson JB, Chand A, Gebeshuber IC, Kindt JH, Richter M, Hansma HG, Hansma PK [22] (2000) Nature Struct Biol 7:644 [22] © 2000, Nature Publishing Group[rs1]

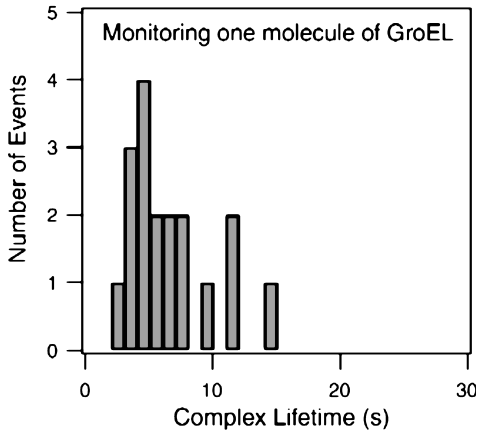

Fig. 2.9. Histogram of measured GroEL–GroES complex lifetime in the presence of Mg-ATP. Individual GroES molecules attach to and then separate from the same GroEL molecule 18 times during an observation period of about 120 seconds. Note the absence of events with lifetimes < 2 seconds. This is interesting in itself, telling us about the GroEL-GroES complex lifetime on the single molecule level, and furthermore indicates gentle measuring, since strong disturbance of complex formation by the cantilever would also lead to subsecond complex lifetimes. Reprinted with permission from Viani MB, Pietrasanta LI, Thompson JB, Chand A, Gebeshuber IC, Kindt JH, Richter M, Hansma HG, Hansma PK [22] (2000) Nature Struct Biol 7:644 © 2000, Nature Publishing Group

A histogram of the complex lifetime for a single GroEL molecule that was investigated for about 120 seconds is shown in Fig. 2.9. During this time interval, 18 times a complex with GroES has formed. The distribution of complex lifetime peaks near five seconds and the average lifetime is $\sim 7 \pm 1$ s ($n = 18$).

In future application of this kind of single molecule studies with the AFM, misfolded proteins could well be involved and, e.g. the effect of various pharmaceuticals on folding efficiency could be tested.

2.4 Nanodefects on Atomically Flat Surfaces

Most of the small structures currently used in technology are in the micrometer range. One reason for this is silicon micromachining technology, which works fast and at low cost in this regime.

However, needs for increased data-storage density and smaller devices call for nanometer-sized structures.

Nanofabrication techniques comprise techniques such as electron beam and nano-imprint fabrication, epitaxy and strain engineering, scanning probe techniques, as well as self-assembly and template manufacturing [32].

Nanotransfer printing is a more recent high-resolution printing technique, which uses surface chemistries as interfacial "glues" and "release" layers to control the transfer of solid material layers from stamp relief features to a substrate [33].

One important way to produce nanostructures on surfaces involves kinetic sputtering by "fast" ions. However, fast ions unavoidably cause unwanted radiation damage. As opposed to this, potential sputtering (PS), i.e. desorption induced by the potential energy of slow multiply charged ions (MCI), holds great promise for more gentle nanostructuring of insulating surfaces [34, 35].

It can cause high sputter yields even at such low ion impact energies where kinetic sputtering and defect creation in deeper layers is not possible. While the physical mechanisms of PS have been the subject of extensive investigation [36–40], technical applications of slow MCI have so far remained largely unexplored, despite the fact that they provide unique opportunities for etching, ultra-thin film growth and nanostructure fabrication.

The AFM is the microscope of choice for investigating ion induced nanodefects on flat crystals, because of its unprecedented resolution and of the fact that it can also image insulating materials.

2.4.1 Ion Bombardment of Highly Oriented Pyrolytic Graphite (HOPG)

HOPG is used as a diffracting element in monochromators for X-ray and neutron scattering and as a calibration standard for STM and AFM. The graphite surface is easily prepared as a clean atomically flat surface by cleavage with an adhesive tape. HOPG is, therefore, used in many laboratories as the surface of choice for "seeing atoms".

Surface defects in HOPG produced by the impact of individual (singly charged) ions have already been investigated via STM/AFM by a number of groups [41–50 and further references therein].

However, first results were reported only recently for impact of slow multiply charged ions and the effect of the projectile charge state (or potential energy) on the size of the produced nanodefects [51–54].

Moreover, in most previous studies, either STM in air was used or the irradiated samples were transported in air towards STM inspection after ion bombardment. If, e.g., chemical bonds at the surface are broken due to the ion impact, impurities could preferentially adsorb at these sites and thus change the topography of the surface (and the resulting STM image) during contact with air. Therefore, here MCI bombardment has been followed by STM/AFM investigations without breaking the ultra-high vacuum. In this way, possible influences from target surface exposure to air can be ruled out.

Figure 2.10 shows STM and AFM scans of the HOPG surface before bombardment.

The STM image of HOPG bombarded with 800 eV Ar^+ ions reveals a large number of individual nanosized defects as a result of ion bombardment (Fig. 2.11). In AFM scans of the same surface, no significant topographic changes could be detected [55].

For very highly charged projectile ions, surface defects have recently also been observed in AFM studies [53, 54].

Meguro and co-workers found that HCI impact and subsequent treatment either by electron injection from an STM tip or by He-Cd laser irradiation induce a localized

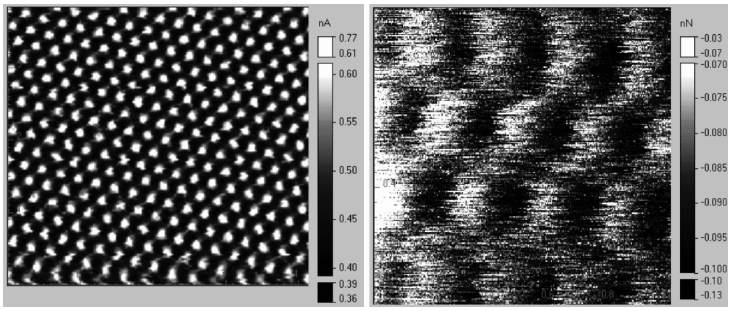

Fig. 2.10. Highly oriented pyrolytic graphite imaged in ultrahigh vacuum with atomic resolution. *Left*: scanning tunneling microscopy image, image size 4×4 nm^2. *Right*: atomic force microscopy image, image size 1×1 nm^2.

transition from sp^2 to sp^3 hybridization in graphite, resulting in the formation of nanoscale diamond-like structures (nanodiamonds) at the impact region [56].

In an investigation of HOPG bombarded with 400 eV Ar^+ and Ar^{8+} ions involving Raman spectroscopy, Hida and co-workers found that the charge state of the ions as well as their mass have an influence on the disordering of HOPG and that the defects introduced by Ar^{8+} are not simple vacancies, but assumed to be vacancy clusters in contrast to their results for Ar^+ irradiation [57].

Several hundred defects from different sample positions have been statistically analyzed for each projectile type (Ar^+, Ar^{8+}, Ar^{9+}).

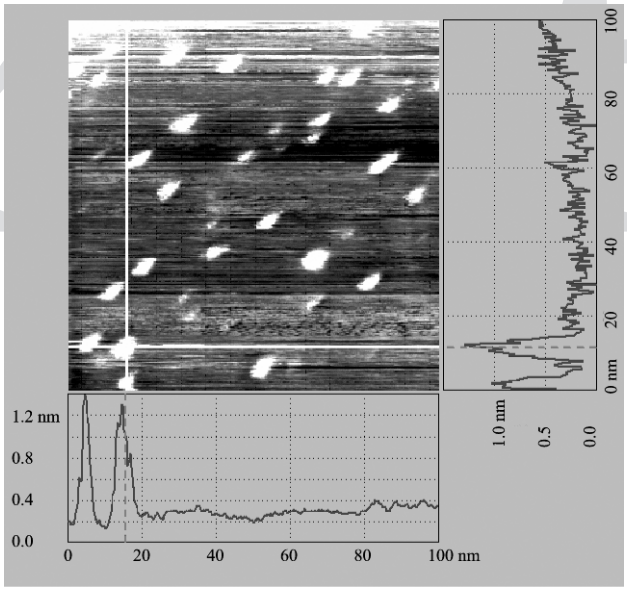

Fig. 2.11. Highly oriented pyrolytic graphite bombarded with 800 eV Ar^+ ions imaged with STM in ultrahigh vacuum. Image size 100×100 nm^2. The ion induced nanodefects are clearly visible

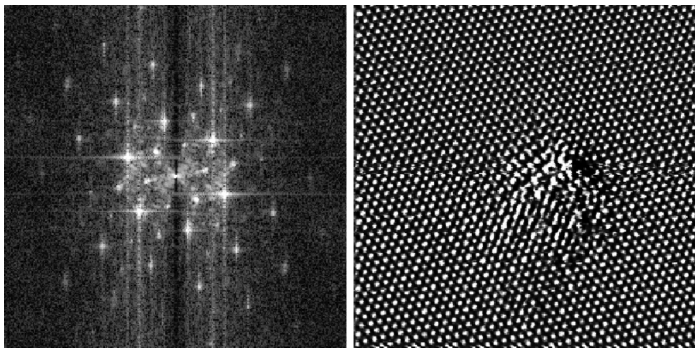

Fig. 2.12. Highly oriented pyrolytic graphite bombarded with 800 eV Ar^+ ions imaged with STM in ultrahigh vacuum with atomic resolution (*right*). Image size $10 \times 10\,nm^2$. The fast Fourier transform (*left*) of the Ar^+ ion-induced defect reveals a $\sqrt{3} \times \sqrt{3}R30°$ surface: the ion induced features are larger than the features from the HOPG lattice and they are rotated with respect to them by 30 degrees

Figure 2.12 (right trace) shows the enlarged STM image of a typical defect on HOPG created by the impact of a single Ar^+ ion of 800 eV kinetic energy

The only surface defects found in the STM images are "protrusions" (hillocks) with a mean lateral size of 0.8–1.25 nm and an average equivalent height of 0.22 nm. They are randomly dispersed on the originally flat surface. Their area density is in good agreement with the applied ion dose, implying that nearly every single ion impact has caused one protrusion. A $\sqrt{3} \times \sqrt{3}R30°$ surface, as characteristic for interstitial defects in HOPG [58–60], surrounded by undisturbed surface parts is observed in the vicinity of most defects (see Fig. 2.12). Scanning with the AFM down to atomic resolution on the irradiated surface did not show any significant topological changes due to ion bombardment. Therefore, we conclude that the nanodefects produced by slow ion impact are of electronic rather than of topographic nature.

For impact of singly charged ions, our findings are in good agreement with previous observations [45, 59].

As a remarkable result, however, it was found that the measured mean diameter of the "hillocks", and to a somewhat lesser extent their "height", increase with the projectile charge state [55]. In a careful STM study, Hahn and Kang [59] showed that generally two kinds of defects in HOPG are created by low energy (100 eV) Ar^+ bombardment, namely carbon vacancy defects (VDs) and interstitial defects (IDs) formed by trapping the projectile beneath the first carbon plane.

Both types of defects are detected as protrusions in the STM topographic image. The dangling bonds at the VD site cause an enhancement of the local charge density-of-states (CDOS) near the Fermi energy, seen as a protrusion in the STM image [59].

The protrusion observed in the STM image at ID sites results from a small geometric deformation of the graphite basal plane due to the trapped projectile (not large enough to be visible in our AFM scans) and an apparently larger electronic defect due to an increased CDOS. A $\sqrt{3} \times \sqrt{3}R30°$ surface was reported [59] only for IDs but not for VDs. From this $\sqrt{3} \times \sqrt{3}R30°$ superlattice structure also

observed in our experiments (see Fig. 2.12), we therefore conclude that the majority of the "hillocks" observed are due to IDs, or VDs created along with IDs. The strong increase of the lateral protrusion size with increasing charge state of the projectile ion is interpreted as a "pre-equilibrium" effect of the stopping of slow multiply charged ions in HOPG, as has so far only been observed for higher charge states [46].

Although MCI are converted already into neutral hollow atoms (i.e., an atom whose inner shells remain essentially unoccupied) during their approach towards the surface, their captured electrons remain in highly exited states until surface impact, where they are gradually peeled off and replaced by conduction band electrons forming a partial screening cloud around the MCI [61].

Before final deexcitation of the hollow atom can take place within the solid, reduced screening should result in a strongly increased energy loss of the projectiles. According to SRIM-2000 (© IBM) calculations [62], the mean range of 150 eV Ar projectiles in HOPG is about two monolayers. An increased stopping and straggling of the higher charged Ar projectiles would lead to IDs located closer to the surface, as well as to more VDs due to a higher momentum transfer to the carbon atoms of the first plane. Because of the extreme surface sensitivity of STM, this pre-equilibrium effect in the stopping power is not masked by (equilibrium) bulk effects and is apparently observable with unprecedented clearness.

Extending pertinent work by other groups with singly charged ions only, our combined STM/AFM studies revealed nanodefects that comprise a disturbance of the electronic density-of-states of the surface rather than its topography.

Whereas the size of these defects increases with the ion charge (here up to $q = 9$), as expected for any conducting target surface they showed no evidence for potential sputtering.

For more detailed information on these studies, see [52, 55].

2.4.1.1 Revealing the Hidden Atom in Graphite by Low-Temperature AFM

Despite the proverbial ease of imaging graphite by STM with atomic resolution, every second atom in the hexagonal surface unit cell remains hidden, and STM images show only a single atom in the unit cell.

The reason for this is that the tunneling current is not a function of the surface topography, but of the local electronic structure. On the graphite surface, there are two different types of carbon atoms in the basal plane, as distinguished by the presence (α) or absence (β) of a carbon atom in the plane immediately below the surface. The α atoms are located directly above another α atom, in the layer directly underneath, the β atoms are located above a hollow site. These local electronic structure variations imply that the STM can only detect every other atom on the graphite surface. Consequently, an alternative imaging method is required to detect the "hidden" α atoms on the graphite surface [63].

Also in contact-mode AFM images of graphite the quasi-atomic resolution images show only one protrusion per unit cell [64].

Recent progress in dynamic AFM allows researchers to routinely achieve true atomic resolution on conductors and insulators [65, 66], but once again only one

maximum within a hexagonal unit cell of the graphite surface was obtained in the attractive noncontact mode [67].

In 2003, Hembacher and co-workers presented measurements with a low-temperature atomic force microscope with pico-Newton force sensitivity that reveal the hidden surface atom [68].

The instrument used in this investigation is a combined ultrahigh vacuum (UHV) STM/AFM to simultaneously probe the charge density at the Fermi level and the total charge density of graphite by recording tunneling currents and forces, respectively. The instrument is immersed in a liquid He bath cryostat, yielding a sample temperature of 4.89 K and exceptionally low thermal drifts of about 0.02 nm/h (at room temperature, even with drift correction, currently 2–10 nm/h are achieved). To protect the microscopy from external vibrations, the setup is built on a foundation with a mass of 30,000 kg.

In their dynamic AFM images of graphite, recorded at small oscillation amplitudes and with weak repulsive forces, both the α atoms and the β atoms are detected. The reason for this is that the repulsive forces utilized in AFM involve different electrons in the tungsten tip than in the STM mode.

Revealing the hidden atoms in graphite by means of room-temperature AFM might become possible with miniaturized AFMs based on nano- or microelectromechanical systems (NEMS/MEMS) technology (since they show small drift). In such an instrument, the operating frequency could be commensurately increased and there would be no need for a 30,000 kg fundament [63].

2.4.2 Bombardment of Single Crystal Insulators with Multicharged Ions

Systematic STM/AFM investigations on nanoscopic defect production at atomically clean insulator surfaces of Al_2O_3 after bombardment by slow (impact energy $\leq$ 1.2 keV) singly and multiply charged ions under strict UHV conditions is the topic of this section.

It will be demonstrated that on monocrystalline insulator surfaces, well-defined topographic features of typically nm extensions are produced ("potential sputtering"). For Al_2O_3, there exists a clear dependence of the defect size on the projectile ion charge. These results are discussed in view of possible new nanoscopic surface structuring and modification methods for which the kinetic projectile energy plays only a minor role.

Impact of slow ions on solid surfaces can give rise to inelastic processes that modify the geometric and electronic structure at and below the surface, cause emission of electrons and photons as well as neutral and ionized target particles (atoms, molecules, clusters), remove surface-adsorbed material and lead to projectile neutralization. The transfer of electrons between surface and projectile possibly acts as precursor for the above-mentioned processes and makes them proceed irrespective of the kinetic projectile energy.

The importance of such "electronic" processes increases with multicharged projectile ions and their role is elucidated when slow ions of the same kinetic energy, but with different charge states are applied as projectiles.

For certain insulator surfaces, the impact of slow multicharged ions (MCIs) Z^{q+} gives rise to considerably stronger ablation than the well-established kinetic sputtering by neutral or ionized projectiles. First experimental evidence for this PS was reported for alkali-halide surfaces and explained by "Coulomb explosion" [69], i.e. the creation of small positively charged surface spots from the rapid electron capture by impinging MCI, and the subsequent ablation because of strong mutual target ion repulsion.

"Coulomb explosion" was also invoked in order to explain AFM observations of blister-like defects on mica samples produced by highly charged ions Z^{q+} (kinetic energy 1–3 keV/atomic mass unit) [38, 70].

However, studies for impact of slow ($\leq$ 1 keV) MCI on thin polycrystalline films of alkali-halides (LiF, NaCl) and Al_2O_3 deposited on quartz microbalance crystals [71] suggested a different explanation for PS, namely defect-stimulated desorption induced by very efficient electron capture [37].

It has been established that such desorption processes are induced by electrons (electron stimulated desorption, ESD) or photons (photon stimulated desorption, PSD) on such materials where self-trapping of specific crystal defects proceeds via electron–phonon coupling in the crystal lattice [72].

However, such defect trapping as the prerequisite for PS may also be caused or at least supported by the kinetic projectile energy ("kinetically assisted PS" [39]), which could also explain some PS-like effects reported for target species where no electron–phonon coupling can take place, i.e. for semiconductors like Si and GaAs [70]. In any case, for slow ion impact, the self-trapping mechanism is most relevant for PS. Consequently, for metal and semiconductor surfaces no slow MCI-induced PS can be observed, so far [73].

As the surface region from which a slow MCI does capture electrons should be rather small (nm extensions), it is probable that the surface defects caused by PS are of similar size. In order to study such defect structures, we applied AFM in UHV on monocrystalline target surfaces of insulator species for which PS by slow MCI impact has already been demonstrated on polycrystalline thin films [39, 71, 73].

The results for Al_2O_3 presented below are of possible interest for nanostructuring these surfaces.

Observations of slow ion-induced nanodefects on different atomically clean target surfaces were performed under strict UHV conditions with a combined AFM/STM instrument (UHV-AFM/STM, OMICRON Nanotechnology GmbH, Germany). Nanodefects were looked for on freshly prepared surfaces of sapphire *c*-plane $Al_2O_3(0001)$ after irradiation with low doses of slow singly and multiply charged ions. In order to avoid disturbing noise from an ion irradiation chamber directly attached to the AFM/STM instrument, a transportable UHV vault for target transfer, which was alternatingly coupled via UHV locks to the target ion irradiation chamber and the AFM/STM was used. This procedure kept the target surfaces under permanent UHV conditions after initial cleaning, thermal annealing, and during subsequent slow ion irradiation until completion of the AFM/STM inspection. Ion irradiation of the insulator surfaces was accompanied by low-energy ($\leq$ 4 eV) electron flooding to compensate for surface charge-up, which otherwise strongly inhibits AFM observation or makes it even impossible. The electron gun was arranged at 2 cm distance

to the sample. All AFM observations were made in the contact mode, with the base pressure in the AFM/STM chamber kept at about 10^{-10} mbar during measurements.

The singly and multiply charged ions for target irradiation have been extracted from a 5 GHz electron cyclotron resonance ion source [74], magnetically analyzed and guided via electrostatic lenses to the UHV irradiation chamber. The ions were decelerated in front of the target surface to their desired impact energy ($\leq$ 1.2 keV). Uniform irradiation was assured by rapidly scanning the ion beam across the target surface by means of deflection plates.

2.4.2.1 Production of Slow Ion-Induced Surface Defects on Al_2O_3 Insulator Targets

Polished $Al_2O_3(0001)$ *c*-plane single crystals (TBL Kelpin, Neuhausen, Germany) were CO_2 snow cleaned (to remove micrometer and submicrometer particles and hydrocarbon-based contamination) and then annealed in UHV for 3 h at 400 °C. This preparation technique yields very flat crystal surfaces.

AFM contact mode studies on 14 samples prepared by the standard preparation technique revealed a root mean square (rms) roughness of 0.093 $\pm$ 0.06 nm rms. Bombardment with Ar ions of different charge states and kinetic energies (500 eV Ar^+ and Ar^{7+}, 1.2 keV Ar^+, Ar^{4+} and Ar^{7+}) results – as seen in AFM contact mode – in hillock-like nanodefects (see Fig. 2.13).

The ion-induced defects on the sapphire single crystal surface can be removed by annealing at 450 °C for 5 h. The density of nanodefects does not directly correspond with the applied ion dose: an ion dose of 5×10^{12} ions/cm^2, which is equivalent to five ions per 10 nm $\times$ 10 nm, leads to a rather small, however reproducible, density of defects on the sapphire surface: about 10 nanodefects per 1000 nm $\times$ 1000 nm can be observed after bombardment in the energy range reported here. This is equivalent

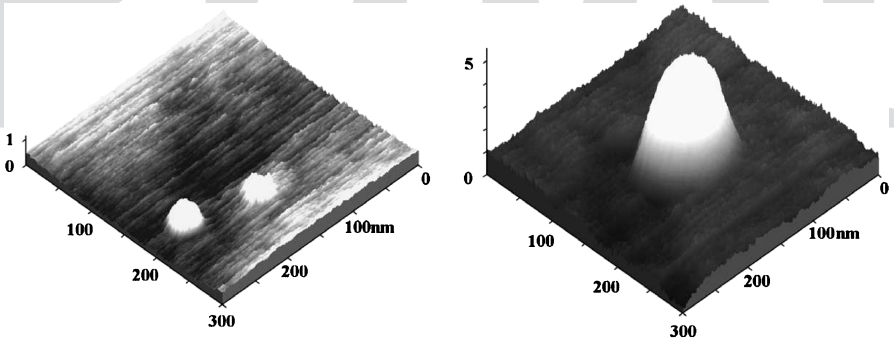

Fig. 2.13. UHV AFM contact mode image of sapphire (Al_2O_3, *c*-plane 0001) bombarded with 500 eV Ar^+ (*left image*) and Ar^{7+} (*right image*) ions. The nanodefects induced by Ar^{7+} ions (which have the same kinetic but higher potential energy than the Ar^+ ions) are considerably higher and wider than those caused by singly charged ions. The defects are real topographic features; the units on the three axes are nanometers. Reprinted with permission from Gebeshuber IC, Cernusca S, Aumayr F, Winter HP (2003) Int J Mass Spectrom 229:27 [55] © 2003, Elsevier Science B.V

to a dose to defect ratio of 5000. More detailed experiments with different ion doses are needed. Analysis of the statistics of random impacts will clarify how many individual ion impacts are needed to form a visible nanodefect on the insulator surface.

A possibly similar migration and subsequent recombination of point defects at the surface has previously been reported for silicon bombarded by 5 keV He ions above 160 K [75].

In fact, the only case where the number of defects corresponded fairly well to the applied ion dose was for the conducting HOPG samples (see Sect. 2.4.1).

The Al_2O_3 *c*-plane proved to be the insulator surface showing most clearly a dependence of the ion bombardment induced defects with the kinetic energy and charge states of the projectiles. 500 eV Ar^+ ions produce defects that are about 1 nm high (Fig. 2.13) and have lateral dimensions of some tens of nanometers (one should keep in mind that the height is more accurately measurable with the AFM than lateral dimensions), whereas the defects produced by 500 eV Ar^{7+} ions are several nanometers high (Fig. 2.13) and show lateral dimensions of about 100 (!) nanometers. At higher kinetic energy the differences in the slow ion-induced nanodefects on the sapphire c-plane became even more distinct.

1.2 keV Ar^+-induced defects are up to about 8 nm high and their width is some 10 nm. For a higher charge state such as Ar^{4+}, two different kinds of defects occurred on the sapphire surface.

They have about the same height, but their lateral dimensions vary considerably: some are nearly 200 nm wide, whereas the smaller defects are only about 50 nm wide.

The height of both kinds of defects is about 2 nm. For Ar^{7+}, only one kind of defect was visible in the AFM images, with about 50 nm diameter and about 2 nm height (for a more detailed description of these results and for similar investigation on SiO_2 surfaces, see [55]).

Al_2O_3 is, therefore, a good candidate for PS-induced nanostructuring. This material is relevant for applications in microelectronics and nanotechnology.

2.5 Subatomic Features

In this section, the detection of atomic orbitals and single electron spins by means of SMP is described. In many cases, sophisticated signal acquisition techniques have to be applied, and the instruments have to be operated at very low temperature, since extremely small drift is required.

2.5.1 Atom Orbitals

Silicon and tungsten are the two chemical elements that already have been investigated with SPM regarding their atomic orbitals.

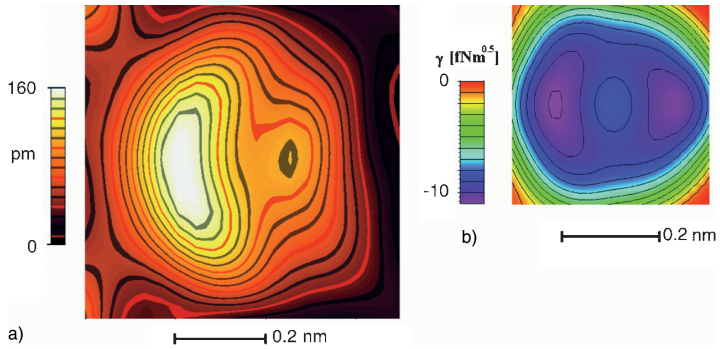

Fig. 2.14. Refined calculations of the normalized frequency shift of a single adatom on the reconstructed silicon (111)-(7 × 7) surface (*right*) performed by the Giessibl group, showing striking similarities with the experimental images (*left*). Reprinted with permission from Hug HJ, Lantz MA, Abdurixit A, van Schendel PJA, Hoffmann R, Kappenberger P, Baratoff A, Giessibl FJ, Hembacher S, Bielefeldt H, Mannhart J (2001) Science 291:2509 [78] © AAAS 2001

2.5.1.1 Silicon (111)-(7 × 7) Surface

Publications concerning the imaging of subatomic features with the AFM started in the year 2000, when Giessibl and co-workers published their paper on imaging of subatomic features on the reconstructed silicon (111)-(7 × 7) surface [76]. For a review on semiconductor surface reconstruction, see [77].

A scientific discussion, in which Hug and co-workers questioned this result by proposing that the subatomic features are caused by a feedback artifact, followed this publication [78].

In the course of this argument, Giessibl and co-workers presented refined calculations, showing striking similarities to the experimental images (see Fig. 2.14).

In 2003, Huang and co-workers presented a theoretical work demonstrating the feasibility of seeing atomic orbitals on the Si(111)–(7 × 7) surface with AFM [79].

2.5.1.2 Tungsten

In 2004, Giessibl and co-workers finally ended this discussion by presenting images of an individual tungsten atom by AFM at a resolution of 77 pm [80]. The diameter of a tungsten atom is 274 pm. Four distinct peaks that are attributed to highly localized electron clouds can be identified (Fig. 2.15).

The experiment was performed in UHV at a temperature of about five Kelvin. The microscope was isolated from vibrations by a 30 t foundation and from sound and electromagnetic stray fields by a metal chamber.

In contrast to STM (which only probes the most loosely bound electrons with energies at the Fermi level) AFM can resolve the charge density variations within a single atom, because the forces between the AFM tip and the sample are of electrostatic nature.

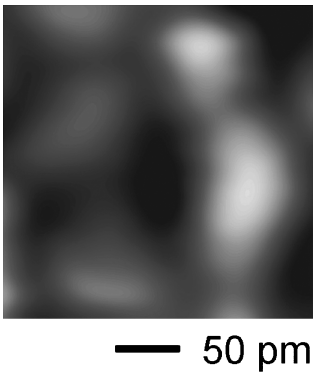

Fig. 2.15. UHV low temperature (5 K) AFM constant-height mode image reveals four-fold symmetry in the amplitudes of the higher harmonics signal (centered close to the maximum of the tunneling current, data not shown). Reprinted with permission from Hembacher S, Giessibl FJ and Mannhart J (2004) Science 305:380 [80] © 2004, AAAS[TS-1]

The electron structure originates from the quantum-mechanical nature of tungsten bonding: tungsten develops a body centered cubic crystal structure such that every tungsten atom is surrounded by eight nearest neighbor atoms, causing "arms" of increased charge density which point to the next neighbors. Four of these highly localized electron clouds are visible on surface atoms.

The role of tip and sample was switched in the experiment: the front atom in a sharp tungsten tip was imaged by a light carbon atom of a graphite surface. The reason a light atom was used for probing was to minimize image blurring, since the mapping of one atom with another atom always involves a convolution of the electronic states. The tunneling current is confined to the top atom because of the sharp increase of tunneling probability with decreasing distance.

Instead of measuring static deflections or frequency changes, higher harmonics triggered by forces between the tip and the sample are recorded in this technique. These higher harmonics are much more sensitive to short-range interactions than static deflections or frequency changes.

2.5.2 Single Electron Spin Detection with AFM and STM

Single-spin detection is a vital goal for read-out in quantum computing, and single nuclear spin detection could solve the problem of how to distinguish between materials at the atomic level.

Several research groups have reported various single spin-detection methods [81–88].

In 1989, Manassen and co-workers presented the first direct observation of the precession of individual paramagnetic spins on partially oxidized silicon (111) surfaces [81].

They used an STM to detect the modulation in the tunneling current at the Larmor frequency. The Larmor frequency is the frequency at which magnetic resonance can be excited. It is given by the Larmor equation, which states that the resonant frequency is proportional to the overall (macroscopic and microscopic) magnetic field. Balatsky and Martin presented the theoretical explanation of this result [89] in 2001.

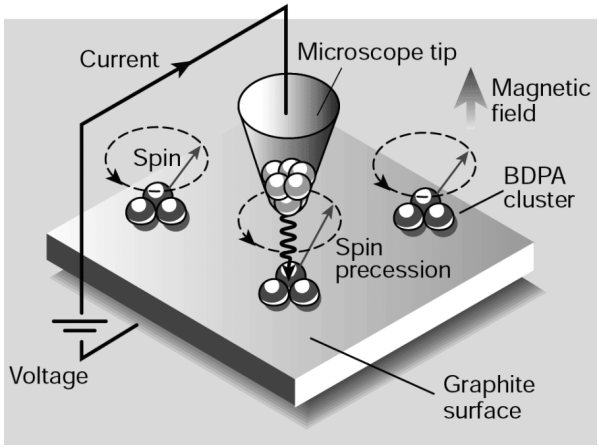

Fig. 2.16. Spin detection through the union of high-resolution microscopy and resonance techniques. The sample is a HOPG surface coated with clusters of organic BDPA molecules. In the applied magnetic field, the electron-spin vectors associated with free radicals in the molecules precess at a certain frequency. The STM tunneling current is modulated at the precession frequency. Detecting the modulation effectively measures electronic spin in the molecule. Reprinted with permission from Manoharan HC (2002) Nature 416:24 [90] © Nature Publishing Group, 2002

In 2002, Durkan and Welland published an article that essentially reproduced this experimental result with a different sample: BDPA (a, g-bisdiphenylene b-phenylallyl) on HOPG [82].

The idea of combining magnetic resonance (MR) with force microscopy in magnetic resonance force microscopy (MRFM) was published as a concept in 1991 [91].

Sidles settled on force microscopy because the performance of induction coils, the detectors in conventional MR, scales unfavorably with size. Shrinking the coil to detect a single spin reduces the signal irretrievably below noise. A force microscope, on the other hand, becomes more sensitive the smaller it gets.

In 1992, Rugar and co-workers demonstrated that the force exerted by 10^{12} electron spins could be detected at room temperature with a conventional cantilever for AFM [92].

Since then they have improved their spin detection limit by 12 orders of magnitude:

MRFM was proposed as a means to improve detection sensitivity to the single-spin level, and thus enable 3D imaging of (bio)molecules with atomic resolution [93, 94].

MRFM is essentially a combination of 3D magnetic resonance imaging (MRI) with the unprecedented resolution of AFM.

For an overview on MRFM, see Hammel and co-workers, 2003 [95] and for the theory of spin relaxation in MRFM, see Mozyrsky et al. 2003 [96].

In the year 2004, the force exerted by a single electron spin was measured by MRFM ([88], Fig. 2.17).

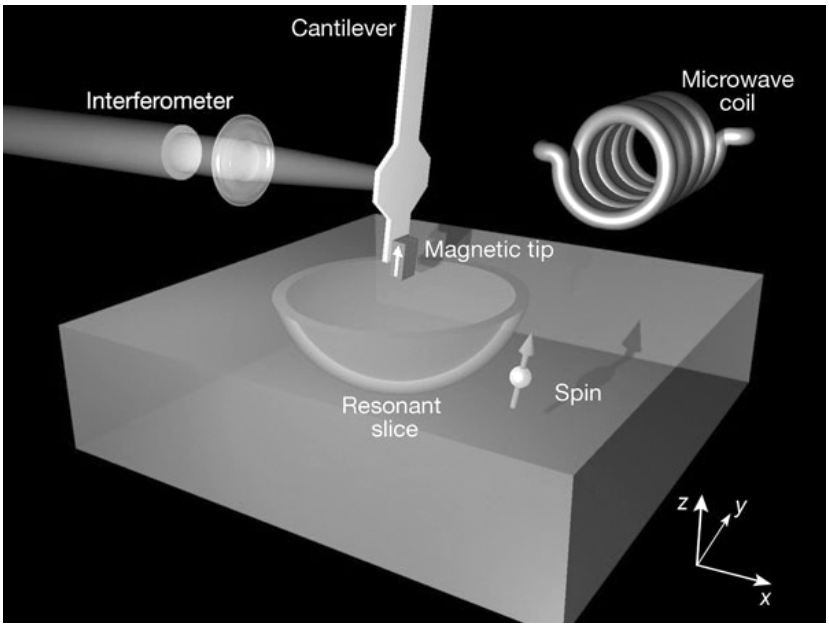

Fig. 2.17. A wiggling cantilever with a tiny CoSm magnet is the key element of a magnetic resonance force microscope. Elaborated signal acquisition makes it possible to detect a single electron spin dozens of atomic layers beneath the surface. In this way, scanning probe microscopy left the surface regime. Perhaps even atomic resolution images of molecules beneath the surface might be possible in the near future. Reprinted with permission from Rugar D, Budakian R, Mamin HJ, Chui BW (2004) Nature 430:329 [88] © Nature Publishing Group, 2004

The force detected in the Rugar 2004 experiment is a million times smaller than the forces usually encountered in AFM (van der Waals forces, electrostatic forces). The single electron spin was buried 250 nm below the surface of an irradiated vitreous silicon sample and exerted a force of 2 aN (2×10^{-18} N).

The sample had been prepared by irradiation with a 2 Gy dose of ^{60}Co gamma rays, producing a low concentration of Si dangling bonds containing unpaired electron spins known as E' centers. Unpaired electrons and many atomic nuclei behave like tiny bar magnets. Estimated spin concentration was between 10^{13} and 10^{14} cm^{-3}. The experiment was performed at 1.6 K in a small vacuum chamber that fits within the bore of a superconducting magnet. The low operating temperature minimizes thermal noise and reduces the relaxation rate of the spins.

The force exerted by a single electron spin is the smallest ever detected. Currently, the smallest volume elements in an image must contain at least 10^{12} nuclear spins for MRI-based microscopy [97], or 10^7 electron spins for electron spin resonance microscopy [98].

The cantilever used in the experiment is only 100 nm thick and had to be aligned vertically to the surface. In the conventional AFM configuration with the cantilever parallel to the surface, van der Waals forces and electrostatic forces would make it stick on the surface. Directly on the cantilever a strong 150 nm wide CoSm magnet

is attached. It generates a field gradient of 200,000 T/m. The cantilever is slowly scanned over the surface. A laser interferometer records the cantilever deflections and sophisticated measurement signal acquisition techniques are needed for successful single spin detection. The strong magnetic field gradient allows for distinguishing magnetic resonance signals arising from different spatial locations, enabling accurate spin localization. By scanning the tip over the sample, a local magnetic resonance force is detected, which corresponds with a spatial resolution of about 25 nm. This spatial isolation of the signal is also the main argument that a single spin is being detected. Currently this method is very slow. As Stokstad mentions in his "Science News of the Week" article on the Rugar experiment, scanning a 170 nm stretch of the irradiated silicon sample took several weeks [99].

MRFM could serve as an invaluable tool for the implementation of a spin-based solid state quantum computer. It provides an attractive means for addressing the characterization and control of the fabrication process of the device during its construction and the readout of the computational result [**?**, 100].

If developed further, the MRFM technique could prove useful for investigating the atomic structure inside materials used in the electronics industry and to image biomolecules – such as proteins – at atomic resolution. However, to reach this goal, nuclear spins have to be detected. Nuclear spins are harder to detect than electron spins, because a proton's magnetic moment is 658 times smaller than that of an electron.

2.6 Conclusions and Outlook

In this review, we have presented scanning probe microscopy across dimensions from large samples like single cells, via single biomolecules and nanometer small ion induced defects on crystal surfaces to subatomic features like electronic orbitals and single electron spins.

Scanning probe microscopy is on its way to a standard laboratory method: subatomic features can be imaged, and with magnetic resonance force microscopy it has even left the two-dimensional surface regime. Perhaps in the not too distant future 3D-imaging of (complex) molecules, at surfaces or in the bulk state, with atomic resolution might become possible with these powerful techniques. The 3-D MRFM would also deliver chemical specific information because each magnetic nucleus has a unique gyromagnetic ratio.

Acknowledgements. Part of this work was supported by the Austrian FWF and was carried out at Vienna University of Technology.

Part of this work was funded by the "Austrian Kplus-Program" and was done at the "Austrian Center of Competence for Tribology", AC^{2}T Research GmbH.

References

1. Radmacher M (2006) Investigating life cells by atomic force microscopy. In: Bhushan B, Fuchs H (eds) Applied scanning probe methods II, Springer, Berlin Heidelberg New York, p xxx TS^2

TS^2 Please provide a page-number.

Editor's or typesetter's annotations (will be removed before the final TEX run)

2. Round FE, Crawford RM, Mann DG (1990) Diatoms: biology and morphology of the genera, Cambridge University Press
3. Hecky RE, Mopper K, Kilham P, Degens ET (1973) Marine Biol 19:323
4. Gordon R, Sterrenburg F, Sandhage K (guest eds) (2005) Diatom nanotechnology, special issue J Nanosci Nanotechnol
5. Gebeshuber IC, Thompson JB, Del Amo Y, Stachelberger H, Kindt JH (2002) Mat Sci Technol 18:763
6. Werner D (1977) The biology of diatoms, University of California Press
7. Gordon R, Drum RW (1994) Int Rev Cytol 150:243
8. Linder A, Colchero J, Apell H-J, Marti O, Mlynek J (1992) Ultramicrosc 42-44:329
9. Almqvist N, Delamo Y, Smith BL, Thomson NH, Bartholdson A, Lal R, Brzezinski M, Hansma PK (2001) J Microsc 202:518
10. Higgins MJ, Crawford SA, Mulvaney P, Wetherbee R (2002) Protist 153:25
11. Gebeshuber IC, Kindt JH, Thompson JB, Del Amo Y, Stachelberger H, Brzezinski M, Stucky GD, Morse DE, Hansma PK (2003a) J Microsc 212:292
12. Higgins MJ, Sader JE, Mulvaney P, Wetherbee R (2003a) J Phycol 39:722
13. Higgins MJ, Molino P, Mulvaney P, Wetherbee R (2003b) J Phycol 39:1181
14. Lee Y, Ding Z, Bard AJ (2002) Anal Chem 74:3634
15. Hamm CE, Merkel R, Springer O, Jurkojc P, Maier C, Prechtel K, Smetacek V (2003) Nature 421:841
16. Arce FT, Avci R, Beech IB, Cooksey KE, Wigglesworth-Cooksey B (2004) Biophys J 87(6):4284
17. Solomon B, Taraboulos A, Katchalski-Katzir E (2002) Conformational diseases: a compendium based on the 1st international workshop on conformational diseases, S Karger Pub, Tunbridge Wells, UK
18. Dobson CM (2002) Nature 418:729
19. Dobson CM (2003) Nature 426:884
20. Greulic KO (2004) Curr Pharmac Biotech 5:243
21. Viani MB, Pietrasanta LI, Thompson JB, Chand A, Gebeshuber IC, Kindt JH, Richter M, Hansma HG, Hansma PK (2000) Nature Struct Biol 7:644
22. Walters DA, Cleveland JP, Thomson NH, Hansma PK, Wendman MA, Gurley G, Elings V (1996) Rev Sci Instrum 67:3583
23. Viani MB, Schäffer TE, Chand A, Rief M, Gaub HE, Hansma PK (1999a) J Appl Phys 86:2258
24. Viani MB, Schäffer TE, Paloczi GT, Pietrasanta LI, Smith BL, Thompson JB, Richter M, Rief M, Gaub HE, Plaxco KW, Cleland AN, Hansma HG, Hansma PK (1999b) Rev Sci Instrum 70:4300
25. Braig K, Otwinowski Z, Hegde R, Boisvert DC, Joachimiak A, Horwich AL, Sigler PB (1994) Nature 371:578
26. Hunt JF, Weaver AJ, Landry SJ, Gierasch L, Eisenhofer J (1996) Nature 379:37
27. Boisvert DC, Wang J, Otiwonowski Z, Horwich AL, Sigler PB (1996) Nature Struct Biol 3:170
28. Xu Z, Horwich AL, Sigler PB (1997) Nature 388:741
29. Chen S, Roseman AM, Hunter AS, Wood SP, Burston SG, Ranson NA, Clarke AR, Saibil HR (1994) Nature 371:261
30. Roseman AM, Chen S, White H, Braig K, Saibil HR (1996) Cell 87:241
31. Ziaie B, Baldi A, Atashbar MZ (2004) Introduction to micro/nanofabrication In: Bhushan B (ed) Springer handbook of nanotechnology. Springer, Berlin Heidelberg New York, p 147

32. Rogers JA (2004) Stamping techniques for micro and nanofabrication: methods and applications. In: Bhushan B (ed) Springer handbook of nanotechnology. Springer, Berlin Heidelberg New York, p 185
33. Arnau A, Aumayr F, Echenique PM, Grether M, Heiland W, Limburg J, Morgenstern R, Roncin P, Schippers S, Schuch R, Stolterfoht N, Varga P, Zouros TJM, Winter HP (1997) Surf Sci Rep 27:113
34. Winter HP, Aumayr F (2002) Europhys News 6:215
35. Sporn M, Libiseller G, Neidhart T, Schmid M, Aumayr F, Winter HP, Varga P, Grether M, Niemann D, Stolterfoht N (1997) Phys Rev Lett 79:945
36. Aumayr F, Burgdörfer J, Varga P, Winter HP (1999) Comm Atom Molecul Phys 34:201
37. Schenkel T, Hamza AV, Barnes AV, DH Schneider (1999) Progr Surf Sci 61:23
38. Hayderer G, Cernusca S, Schmid M, Varga P, Winter HP, Aumayr F, Niemann D, Hoffmann V, Stolterfoht N, Lemell C, Wirtz L, Burgdörfer J (2001) Phys Rev Lett 86:3530
39. Hayderer G, Schmid M, Varga P, Winter HP, Aumayr F, Wirtz L, Lemell C, Burgdörfer J, Hägg L, Reinhold CO (1999) Phys Rev Lett 83:3948
40. Porte L, de Villeneuve CH, Phaner M (1991) J Vac Sci Technol B 9, 1064
41. Coregater R, Claverie A, Chahboun A, Landry V, Ajustron F, Beauvillain J (1992) Surf Sci 262:208
42. You HX, Brown NMD, Al-Assadi KF (1992) Surf Sci 279:189
43. Mazukawa T, Suzuki S, Fukai T, Tanaka T and Ohdomari I (1996) Appl Surf Sci 107:227
44. Mochiji K, Yamamoto S, Shimizu H, Ohtani S, Seguchi T, Kobayashi N (1997) J Appl Phys 82:6037
45. Reimann KP, Bolse W, Geyer U, Lieb KP (1995) Europhys Lett 30:463
46. Habenicht S, Bolse W, Feldermann H, Geyer U, Hofsäss H, Lieb KP, Roccaforte F (2000) Europhys Lett 50:209
47. Neumann R (1999) Nucl Instrum Meth B 151:42
48. Hahn R, Kang K, Song S, J Jeon (1996) Phys Rev B 53:1725
49. Hahn R, Kang K (1999) Phys Rev B 60:600
50. Minniti R, Ratliff LP, Gillaspy JD (2001) Phys Scr T92:22
51. Hayderer G, Cernusca S, Schmid M, Varga P, Winter HP, Aumayr F (2001) Phys Scr T92:156
52. Terada M, Nakamura N, Nakai Y, Kanai Y, Ohtani S, Komaki K, Yamazaki Y (2004) Observation of an HCI-induced nano-dot on an HOPG surface with STM and AFM In: Rudzikas Z (ed) Abstracts HCI-2004 12th international conference on the physics of highly charged ions, European Physical Society, p 208
53. Terada M, Nakamura N, Nakai Y, Kanai Y, Ohtani S, Komaki K, Yamazaki Y (2004) Nucl Instrum Meth B, to be published TS[3]
54. Gebeshuber IC, Cernusca S, Aumayr F and Winter HP (2003) Int J Mass Spectrom 229:27
55. Meguro T, Hida A, Koguchi Y, Miyamoto S, Yamamoto Y, Takai H, Maeda K, Aoyagi Y (2003) Nuc Instrum Meth B 209:170
56. Hida A, Meguro T, Maeda K, Aoyagi Y (2003) Nuc Instrum Meth B 205:736
57. Hahn R, Kang K, Song S, Jeon J (1996) Phys Rev B 53:1725
58. Hahn R, Kang K (1999) Phys Rev B 60:6007
59. Krasheninnikov AV, Elsin F (2000) Surf Sci 519:454
60. Winter HP, Aumayr F (1999) J Phys B: At Mol Opt Phys 32: R39
61. Ziegler JF, Biersack JP, Littmark U (1985) The stopping and range of ions in matter 1. Pergamon, New York
62. Hersam MC and Chung Y-W (2003) Proc Natl Acad Sci 100:12531
63. Albrecht TR and Quate CF (1988) J Vac Sci Technol A 6:271
64. Morita S, Wiesendanger R, Meyer E (2002) (eds) Noncontact atomic force microscopy. Springer, New York

TS[3] Pleas give any update if available.

Editor's or typesetter's annotations (will be removed before the final TEX run)

65. Giessibl FJ (2003) Rev Mod Phys 75:949
66. Hölscher H, Allers W, Schwarz UD, Schwarz A, Wiesendanger R (2000) Phys Rev B 62:6967
67. Hembacher S, Giessibl FJ, Mannhart J, Quate CF (2003) Proc Nat Acad Sci 100:12539
68. Bitensky IS, Murakhmetov MN, Parilis ES (1979) Sov Phys Tech Phys 25:618
69. Schneider DH, Briere MA, McDonald J, Biersack J (1993) Radiat Eff Def Sol 127:113
70. Hayderer G, Schmid M, Varga P, Winter HP, Aumayr F (1999) Rev Sci Instrum 70:3696
71. Townsend P (1983) In: Behrisch R (ed) Sputtering by particle bombardment II. Berlin, Heidelberg, New York, p 147
72. Varga P, Neidhard T, Sporn M, Libiseller G, Schmid M, Aumayr F, Winter HP (1997) Phys Scr T73:307
73. Leitner M, Wutte D, Brandstötter J, Aumayr F, Winter HP (1994) Rev Sci Instrum 65:1091
74. Bedrossian PJ, de la Rubia TD (1998) J Vac Sci Technol A 16:1043
75. Giessibl FJ, Hembacher S, Bielefeldt H, Mannhart J (2000) Science 289:422
76. Duke CB (1996) Chem Rev 96:1237
77. Hug HJ, Lantz MA, Abdurixit A, van Schendel PJA, Hoffmann R, Kappenberger P, Baratoff A, Giessibl FJ, Hembacher S, Bielefeldt H, Mannhart J (2001) Science 291:2509
78. Huang M, Cuma M, Liu F (2003) Phys Rev Lett 90:256101
79. Hembacher S, Giessibl FJ, Mannhart J (2004) Science 305:380
80. Manassen Y, Hamers RJ, Demuth JE, Castellano AJ jun (1989) Phys Rev Lett 62:2531
81. Durkan C, Welland ME (2002) Appl Phys Lett 80:458
82. Wrachtrup J, von Borczyskowski C, Bernard J, Orritt M, Brown R (1993) Nature 363:244
83. Köhler J, Disselhorst JAJM, Donckers MCJM, Groenen EJJ, Schmidt J, Moerner WE (1993) Nature 363:242
84. Jelezko F, Popa I, Gruber A, Tietz C, Wrachtrup J, Nizovtsev A, Kilin S (2002) Appl Phys Lett 81:2160
85. Elzerman JM, Hanson R, Willems van Beveren LH, Witkamp B, Vandersypen LMK, Kouwenhoven LP (2004) Nature 430:431
86. Xiao M, Martin I, Yablonovitch E, Jiang HW (2004) Nature 430:435
87. Rugar D, Budakian R, Mamin HJ, Chui BW (2004) Nature 430:329
88. Balatsky AV, Martin I (2002) Quant Inf Proc 1:355
89. Manoharan HC (2002) Nature 416:24
90. Sidles JA (1991) Appl Phys Lett 58:2854
91. Rugar D, Yannoni CS, Sidles JA (1992) Nature 360:563
92. Sidles JA (1992) Phys Rev Lett 68:1124
93. Sidles JA, Garbini JL, Bruland KJ, Rugar D, Züger O, Hoen S, Yannoni CS (1995) Rev Mod Phys 67:249
94. Hammel PC, Pelekhov DV, Wigen PE, Gosnell TR, Midzor MM, Roukes ML (2003) Proc IEEE 91:789
95. Mozyrsky D, Martina I, Pelekhov D, PC Hammel (2003) Appl Phys Lett 82:1278
96. Ciobanu L, Seeber DA, Pennington CH (2002) J Magn Reson 158:178
97. Blank A, Dunnam CR, Borbat PP, Freed JH (2003) J Magn Reson 165:11
98. Stokstad E (2004) Science 305:322
99. Berman GP, Doolen GD, Hammel PC, Tsifrinovich VI (2000) Phys Rev B 61:14694
100. Pelekhov DV, Martin I, Suter A, Reagor, DW, Hammel PC (2002) Proc SPIE 4656:1